Received: 18 June 2024 | Revised: 30 July 2024 | Accepted: 31 July 2024

DOI: 10.1002/rcm.9891

RESEARCH ARTICLE

Rapid Communications in Mass Spectrometry WILEY

Metabolipidomic changes induced by dermal nickel penetration determined in an ex vivo porcine ear skin model

Azar Rezaei[1] | Yameera Ganashalingam[2] | Siegfried Schindler[1] | Bernhard Spengler[1] | Cornelia M. Keck[2] | Sabine Schulz[1]

[1]Institute of Inorganic and Analytical Chemistry, Justus Liebig University, Giessen, Germany

[2]Department of Pharmaceutics and Biopharmaceutics, Philipps University Marburg, Marburg, Germany

Correspondence
Sabine Schulz, Institute of Inorganic and Analytical Chemistry, Justus Liebig University, Giessen, Germany.
Email: sabine.schulz@anorg.chemie.uni-giessen.de

Funding information
German Academic Exchange Service-Graduate School Scholarship Programme (DAAD-GSSP), Grant/Award Number: 57450037; Giessen Graduate Center for the Life Sciences GGL

Rational: Nickel is one of humans' most prevalent triggers of allergic contact dermatitis. However, the underlying mechanisms of this allergy still need to be fully understood. One aspect that has yet to be explored is the direct impact of common metal allergens on the skin's metabolites and lipids composition.

Method: Our study employed matrix-assisted laser desorption/ionization mass spectrometry imaging (MALDI MSI) to analyze spatially resolved metabolic alterations induced by nickel exposure. Cross-sections of ex vivo porcine ear skin exposed to increasing nickel (II) ion concentrations (17–167 μg/cm^2) were measured with an AP-SMALDI^5 AF ion source coupled to Q Exactive HF Orbitrap mass spectrometer. Additionally, the penetration of nickel ions into the skin was observed through its pink complexation with dimethylglyoxime under light microscopy.

Results: For nickel ion concentrations up to 84 μg/cm^2, most nickel ions were stopped within the stratum corneum, while only a very small proportion of nickel ions penetrated the viable epidermis and dermis. Stratum corneum locations with high nickel ion concentrations showed a decrease in arginine and ceramides. Furthermore, several phosphatidylcholine and sphingomyelin species were found to be downregulated in the viable epidermis and dermis due to the nickel exposure.

Conclusion: Nickel penetrates at a trace level into the viable skin and induces severe metabolomic and lipidomic changes in the stratum corneum, epidermis, and dermis, indicating a change in the skin (barrier) function. These findings contribute to a deeper understanding of nickel-induced skin allergies and provide a solid foundation for further research.

1 | INTRODUCTION

Allergic contact dermatitis (ACD) is a multifaceted immune reaction triggered by exposure to small molecules in our surroundings. It causes an inflammatory skin condition triggered by exposure to certain organic chemicals and metal ions,[1,2] so-called haptens. This immune response engages the innate immune system and cellular stress responses, initiating crucial skin inflammation necessary for the initial sensitization and subsequent development of ACD. Upon contact, allergens bind to proteins, activating specific T cells that further exacerbate inflammation through their actions.[3] ACD is classified as a delayed-type hypersensitivity reaction (type 4) orchestrated by an individual's immune system in response to exposure to particular small molecules. Sensitization occurs initially when these substances interact with skin proteins, priming the skin for dermatitis upon subsequent encounters during the elicitation phase. ACD accounts for approximately 20% of

contact dermatitis cases, with variations influenced by geographic location, personal practices, and permissible preservatives.[4] Various cell types, including T regulatory cells, play vital roles in regulating and resolving the inflammatory process. Effector cells such as CD4 + and CD8 + T cells, natural killer T cells (NKT), natural killer cells, B cells, and innate lymphoid cells contribute to the diverse clinical symptoms observed in ACD reactions.[5] Previous research has shed light on the cellular and molecular mechanisms of ACD, providing valuable insights into the role of different effector cells and the triggering role of haptens in initiating this immune response.[4] Lipids are critical in ACD, serving essential functions in skin structure and immune responses. Fatty acids contribute to the skin's integrity and function among these lipids. They are integral to forming triglycerides, which store energy and provide cell insulation.[6] In the context of ACD, lipids also participate in various signaling pathways and immune reactions.

Lipid mediators, such as prostaglandins and leukotrienes derived from arachidonic acid, play significant roles in inflammation and immune responses. These bioactive lipids act as signaling molecules by binding to specific receptors on target cells upon local synthesis. Notably, the protein CD36 acts as a sensor for long-chain fatty acids, influencing interorgan signaling and facilitating enhanced dietary fat digestion.[7] The skin is a primary defense mechanism against external threats, including pathogens, chemicals, irritants, and allergens, preventing ACD. However, if these substances penetrate the deeper layers of the skin, they may trigger an immune response, highlighting the crucial role of the skin's barrier function.[8] Disruptions in the stratum corneum, the outermost layer of the epidermis, can lead to atopic dermatitis (AD) by compromising the skin barrier function. Restoring the skin barrier function becomes pivotal in preventing or halting the progression of AD, given that the root cause is believed to lie within the skin barrier itself.[9] Skin barrier dysfunction significantly contributes to ACD by enhancing skin permeability, facilitating the rapid penetration of allergens, and triggering immune responses. AD, closely associated with ACD, exhibits skin barrier defects, including changes in lipid composition and reduced ceramide levels, resulting in compromised barrier function.[10] The lipid bilayer in the stratum corneum, comprising hydrophobic lipids such as ceramides, cholesterol, and free fatty acids, plays a crucial role in maintaining skin hydration and integrity.[10] Alterations in lipid composition, such as shorter chain lengths of fatty acids and ceramides observed in AD skin, further exacerbate skin permeability and contribute to barrier dysfunction.[10] Metals are common culprits for contact allergies, with nickel, cobalt, and chromium traditionally being the most significant offenders. Recently, attention has also been directed towards gold and palladium due to their increasing prevalence of contact allergies.[11]

The prevalence of metal hypersensitivity is strikingly high, affecting approximately 10–15% of individuals, with a higher incidence observed in women (around 10–20% versus 1–3% in men).[12,13] Nickel is the most frequently encountered contact allergen in various studies and clinical observations.[14] Hence, caution should be exercised to avoid potential health risks associated with metal exposure. Several factors influence the ability of a substance to penetrate the skin, including the quantity applied, the exposed area, duration of contact, location on the body, skin thickness and condition, sweating, temperature, humidity, physical activity, gender, race, age, and substance properties.[12] Metal allergies, particularly in the context of ACD,[15] cause skin lipid content changes. By examining the lipid profiles of ex vivo human skin, it was found that nickel, cobalt, and chromium significantly alter the levels of monoacylglycerides (MAG) and diacylglycerides (DAG), resulting in a down-regulation of these lipids upon nickel application in the stratum layers.[16]

Many skin diseases, such as psoriasis, AD, and ichthyoses, are linked to changes in the composition and metabolism of epidermal sphingolipids.[17] Changes in the levels of these sphingolipids in the skin have been associated with various skin disorders, such as inflammatory and allergic reactions. Studies of the lipid composition of diseased skin have indicated a decreased level of ceramide in the stratum corneum and altered ceramide profiles in such conditions.[18] Additionally, it has been reported that AD is associated with lipid composition changes and epidermal organization, suggesting a role for lipids like phosphatidylcholine (PC) in allergic skin conditions.[19] Further research into how metal allergies specifically alter these lipid contents and their interplay with the immune system holds immense potential for unlocking new strategies to manage and prevent conditions like ACD. Another substance important for skin health is arginine, a major component of filaggrin-derived natural moisturizing factors found predominantly in the middle layer of the stratum corneum. It contributes significantly to skin hydration.[20]

Recent technological advancements enabled researchers to track metal movement through skin tissue. Inductively coupled plasma mass spectrometry (ICP MS) allowed researchers to measure nickel permeation through skin depending on different nickel counter ions (sulfate, chloride, nitrate, and acetate) applied as an aqueous salt solution. The study used carefully controlled experimental conditions and ICP MS analysis to measure the steady-state flux of nickel through human stratum corneum isolated through trypsinization.[21]

In another study, Malmberg et al used time-of-flight secondary ion mass spectrometry (ToF SIMS) to investigate the distribution and penetration of nickel in ex vivo human skin. The study found that the highest concentration of nickel ions was in the outer layer of the skin, the stratum corneum, and the upper epidermis. The exposure time was 24 hours. In the 3D constructs, a depth of 500 µm into full-thickness human skin and a depth of approximately 400 µm down into punch biopsies (diameter 8 mm) were observed.[22]

Furthermore, they used ToF SIMS to investigate the penetration of three metal salts, nickel, cobalt, and chromium (III) salts, in ex vivo human skin. The results showed that all three metal salts were mainly accumulated in the stratum corneum, with only trace amounts present in the epidermis.[23]

Researchers have used MALDI MSI to analyze the distribution of lipids in normal ex vivo human skin[24] and skin biopsies taken from patients with Fabry's disease. In Fabry's disease, an accumulation of glycosphingolipids was observed in the skin of affected patients, indicating the potential role of these substances in the disease's pathogenesis.[25] MALDI-MSI was also used to study the spatial distribution of a psoriasis drug (acetretin) in a 3D tissue-engineered

psoriatic skin model, demonstrating the potential of this technique to provide insights into disease mechanisms and drug delivery.[26]

Although ToF SIMS offers high spatial resolution and elemental analysis, reliable identification of complex biomolecules such as lipids is hampered by instrumental mass resolving power and ionization-induced fragmentation of molecular ions. For biomolecules, MALDI MSI is the preferred choice in many dermatological applications, providing the unique capability to analyze biomolecules in their native state without complex labeling. Recent advancements in atmospheric-pressure scanning microprobe matrix-assisted laser desorption/ionization (AP-SMALDI) resulted in a substantial improvement of sensitivity and lateral resolution (down to 1.4 µm laser spot diameter) of the method for visualizing the distribution of various biomolecules within tissues.[27] Moreover, coupling with an orbital trapping mass spectrometer featuring high mass resolution and accuracy allows for reliable biomolecule assignment on the sum formula level, making it ideal for high throughput metabolite profiling.[28] Despite its efficiency in lipidomic and skin disease research, MALDI MSI has not yet been applied to investigate nickel allergy mechanisms. Our study utilized MALDI MSI to detect metabolomic changes after nickel exposure in ex vivo porcine skin sections. Reliable biomolecule identification was achieved by additional analysis of the adjacent tissue sections by liquid chromatography–tandem mass spectrometry (LC-MS/MS). Furthermore, the study used dimethylglyoxime (H_2DMG) to visualize by light microscopy the nickel ion distribution in the skin, revealing insights into its penetration behavior.

2 | METHODS

2.1 | Chemicals

LC–MS grade acetonitrile (ACN) and water (H_2O) were purchased from VWR International, Fontenay-sous-Bois, France. Methanol, ethanol, and trifluoroacetic acid were obtained from Merck, Darmstadt, Germany, isopropanol (IPA) from Chemsolute, Renningen, Germany, and formic acid (FA) from Honeywell, Morris Plains, NJ, USA. Methyl-tert-butyl ether (MTBE), ammonium formate (AF), Mayer's hematoxylin solution, Eosin Y solution, xylene, Eukitt, Dimethylglyoxime (H_2DMG), α-Cyano-4-hydroxycinnamic acid (CHCA), Nickel (II) sulfate hexahydrate, and ammonium hydroxide (28% NH_3 in water) were obtained from Sigma-Aldrich, Steinheim, Germany. Synthetic lipid internal standards were procured from Avanti Polar Lipids (Alabaster, AL, USA) and phosphate-buffered saline (PBS) from Gibco, Carlsbad, CA, USA.

2.2 | Tissue sample preparation

Fresh pig ears (three biological replicates) were obtained from a local slaughterhouse and used within an hour after slaughter. First, the ears were cleansed with lukewarm water at approximately 23–25°C and softly dried using a paper towel with gentle dabbing, avoiding rubbing. Subsequently, examination areas measuring 2 × 2 cm (equivalent to an area of 4 cm^2) on the dorsal side of the ears were identified, ensuring that these skin regions were intact and devoid of any injuries.[29] The hair within these designated areas was meticulously trimmed to a length of approximately 1–3 mm using scissors. Then, Nickel (II) sulfate hexahydrate solutions in water with concentrations of 0%$_w$, 1%$_w$, 5%$_w$, and 10%$_w$ were administered to each examination area. The solutions were evenly distributed using a pipette without any massage. A 30 µL dose of the nickel solution was applied to each 4 cm^2 skin area. Control areas of skin treated with 30 µL water were also prepared. After an incubation period of 2 hours at 32°C, punch biopsies with a diameter of 15 mm were obtained from each examination area. Punch biopsies were preserved without further fixation by freezing at −80°C until further analysis.

2.3 | MALDI MSI sample preparation

Skin cross-sections of 10 µm thickness were created at −25°C using a Microm Sec35p® blade on a micro cryotome (Microm HM 525, Microm International GmbH, part of Thermo Fisher Scientific, Walldorf, Germany) and thaw-mounted onto microscopic glass slides. The quality of the sections was checked using a digital microscope (VHX-5000, Keyence, Japan). Prepared sections were kept at −80°C until analyzed with atmospheric-pressure scanning microprobe matrix-assisted laser desorption/ionization mass spectrometry imaging (AP-SMALDI MSI). For MS imaging analysis, the samples were thawed in a desiccator for 30 minutes. CHCA was used as a matrix at a 30 mg/mL concentration dissolved in ACN/H_2O/trifluoroacetic acid (69.95:29.95:0.1, v:v:v). The matrix was applied using an ultrafine pneumatic sprayer (SMALDIPrep, TransMIT GmbH, Giessen, Germany) as described elsewhere.[30] In brief, 100 µLl matrix solution was applied at a flow rate of 10 µLL/min and a nitrogen pressure of 1 bar.

2.4 | MALDI MSI measurements

Imaging experiments were conducted using a Q Exactive HF orbital trapping mass spectrometer (Thermo Fisher Scientific [Bremen] GmbH, Bremen, Germany) equipped with an autofocusing AP-SMALDI[5] AF ion source (TransMIT GmbH, Giessen, Germany). Desorption and ionization of sample molecules were achieved using 50 UV-laser pulses per pixel at a frequency of 100 Hz. A step size of 10 µm was selected for imaging experiments based on the sample size (region of interest, ROI). The ion injection time was set to 500 ms, the s-lens RF level was adjusted to 100 arbitrary units, and the capillary temperature was maintained at 250°C. An acceleration voltage of 3.0 kV was applied to the sample target. All measurements were conducted in positive-ion mode with a mass resolution of 240,000 at *m/z* 200 and a *m/z* range of 100–1,200 (two microinjections: *m/z* 100–400, *m/z* 400–1,200). Internal mass calibration of each recorded mass spectrum was performed with the lock mass *m/z* 249.9877 corresponding to the matrix ion $[CHCA+Na+K-H]^+$.

2.5 | Nickel staining with H_2DMG

After the MALDI MSI measurements were completed, one µL of 1%$_w$ H_2DMG solution in ethanol and ammonium hydroxide (9.9% [v/v]) was pipetted onto the skin cross-sections. Subsequently, the samples were placed in a desiccator for 15 minutes to complete the complexation reaction.[31] After this time, excess H_2DMG was removed by washing the stained tissue section with 500 µL ethanol. After drying, images of the stained skin cross-sections were taken with a digital microscope (VHX-5000, Keyence, Japan), magnification (250x). For the development and performance evaluation of the nickel staining method, skin-cross sections were thawed in a desiccator for 30 min and immediately stained following the procedure described above. Image processing to obtain grayscale images containing only the $Ni(HDMG)_2$ signal is described in the results section. To determine nickel ion penetration depths, an intensity threshold was applied to $Ni(HDMG)_2$ images to convert them into B&W images in ImageJ software.[32] Then, B&W images were saved as date files and imported into Excel. Subsequently, the number of white pixels representing $Ni(HDMG)_2$ was counted in 5,000 columns per image, and the mean and maximum number of white pixels per column were determined. After the conversion of pixel scale to micrometer scale, calculated numbers equal the mean and maximum penetration depths of nickel ions into the skin. Stratum corneum thickness was determined the same way from B&W image data files as nickel penetration depth, but in this case, B&W images of stratum corneum were generated by cropping the stratum corneum layer from the other tissue layers in the original light microscopic images.

2.6 | H&E staining

H&E staining was performed after nickel staining with H_2DMG to evaluate the histology of the skin cross-sections. The staining process involved rehydration using 100%, 70%, and 40% ethanol and deionized water for 2 minutes each. The samples were then kept in a hematoxylin solution for 12 minutes, followed by 10 minutes in tap water and 5 minutes in deionized water. After 1 minute in eosin Y solution, the samples were dehydrated using deionized water, 40%, 70%, 100% ethanol, and xylene for 2 minutes each. Finally, the samples were covered with Eukitt and a cover slip.

2.7 | LC–MS/MS sample preparation

For LC–MS/MS experiments, the lipid extraction method described elsewhere[33] was slightly modified. After cryo-sectioning, 70 mg of skin homogenate prepared from the remaining tissue was mixed with 100 µL of PBS buffer and 350 µL of methanol. The mixture was vortexed for 1 minute at 1500 rpm. Then, 1 mL of MTBE was added, and the mix was shaken for one hour at 20°C and 1,000 rpm. Then 300 µL H_2O was added to enhance phase separation, mixed for 1 minute at 1000 rpm, and centrifuged for 8 minutes at 13,000 rpm. The organic upper phase (1 mL) was collected and dried under nitrogen flow. The dried samples were stored at −80°C until analysis. Before analysis, the samples were reconstituted with 100 µL of ACN/IPA/H_2O (65:30:5, v:v:v). The extraction process used 100 µL of PBS as an extraction blank and the reconstitution buffer as the blank.

2.8 | LC–MS/MS analysis

The extracted lipids were separated on a UHPLC system (Ultimate 3,000 UHPLC, Thermo Fisher Scientific) equipped with a Kinetex C18 analytical column (Phenomenex, Torrance, CA, USA) (2.1 × 100 mm, 2.6 µm particle size, 100 Å pore size) and detected with an Orbitrap Exploris 480 mass spectrometer. Two mobile phases – phase A and phase B – were used. Phase A comprised a mixture of water and acetonitrile (40:60, v:v), while phase B was a mix of iso-propanol and acetonitrile (90:10, v:v). Both mobile phases contained 10mM ammonium formate and 0.1 vol-% formic acid. The experiment used a 28-minute multi-step gradient from 30% to 100% eluent B (Table S1) to separate the lipids. The flow rate was kept constant at 0.25 mL/min, and the injection volume was 10 µl. The column temperature was set to 50°C, while the autosampler temperature was set to 15°C. The lipidomic datasets were acquired using a data-dependent approach with the top-15 method (full MS/ddMS2, Top15) in positive-ion mode. The Orbitrap Exploris 480 was equipped with a heated electrospray ion source (HESI-II), and settings of data-dependent MS/MS acquisition and the HESI source can be found in Tables S2 and S3.

2.9 | Analysis of the mass spectrometric data

LC–MS/MS data were analyzed using LipidMatch Flow 3.1[34] and MS-DIAL. Individual MALDI MSI data sets were converted to imzML, stitched together, and uploaded to METASPACE. Metabolites and lipids were annotated with a mass tolerance of ± 3 ppm and a false discovery rate of 10% using the databases LIPIDMAPS (12.12.2017), swiss lipids (02.02.2018), HMDB-v4 and BraChem (01–2018). Annotation lists from METASPACE were manually compared with lipid lists obtained from MSDIAL and LipidMatch (LC–MS/MS data). Only those lipids detected by MALDI MSI, which were fully identified with fatty acid assignment by LC–MS/MS, were subjected to further semi-quantitative analysis in SCiLS Lab software (version 2016b, SCiLS GmbH, Bruker Daltonics). There, tissue areas of similar size were defined for each MALDI MSI measurement, and total ion count (TIC)-normalized mean intensities of all identified lipids and metabolites were extracted for those tissue areas. Samples were then divided into control and nickel-treated groups, and multiple t-tests were performed in GraphPad Prism on the semi-quantitative data obtained from the SCiLS Lab. Metabolites and lipids with a *p*-value of less than 0.05 were considered significantly different in the control and nickel-treated groups. The corresponding TIC-normalized MS

images and RGB overlay images of three lipids were downloaded from METASPACE. Relative MALDI MSI intensities for the significantly different molecules were calculated by dividing each sample's mean TIC-normalized intensity by the mean TIC-normalized intensity of the control group. Then, average and standard deviation were calculated within the control and nickel-treated groups and displayed as bar charts with error bars.

3 | RESULTS AND DISCUSSION

Our study employed an ex vivo porcine ear skin model to comprehend the effects of nickel exposure on the skin. The well-known complexation reaction of nickel ions with dimethylglyoxime (H_2DMG) was used here to selectively stain nickel ions in skin cross-sections to track their penetration into the skin by light microscopy. MALDI MSI was used to study the metabolomic and lipidomic profile of control and nickel-treated skin topographically. LC–MS/MS was utilized in parallel to reliably identify lipid species detected by MALDI MSI in the different skin layers.

The workflow of the study is shown in Figure 1. Ex vivo fresh porcine ear skin was organized into 4 cm^2 skin areas, and each area was treated with 30 µl nickel sulfate hexahydrate aqueous solutions of varying concentrations (1%$_w$, 5%$_w$, and 10%$_w$). Following a 2-hour open-air incubation in the oven at 32°C, punch biopsies measuring 15 mm in diameter were obtained and frozen at −80°C for future utilization. Frozen biopsies were sectioned at a thickness of 10 µm at −25°C. After cryo-sectioning, skin cross-sections were covered with matrix by ultrafine spraying of a solution of 30 mg/mL α-Cyano-4-hydroxycinnamic acid (CHCA) in ACN/H_2O/THF (70:30:0.1%, v:v:v). Metabolomic changes induced by nickel treatment were examined in positive-ion mode using an AP-SMALDI^5 AF ion source (TransMIT GmbH, Giessen, Germany) coupled to Q Exactive HF Orbitrap mass spectrometer (Thermo Fisher Scientific, Bremen, Germany). Subsequently, the measured tissue sections were stained with H_2DMG to visualize nickel ion penetration, followed by light microscopy analysis. Afterward, H&E staining was performed to assess tissue morphology by light microscopy. The remaining tissue from cryo-sectioning was ground, and lipids were extracted for LC–MS/MS analysis to identify the fatty acid composition of the lipid species annotated by the METASPACE online platform in the MALDI MSI data sets.

3.1 | Nickel ion penetration into pig ear skin

This study used nickel (II) sulfate hexahydrate in fresh pig ears as a model to simulate metal allergy responses in humans. Pig skin is very similar to human skin in its anatomy and thus is often used to study the effects of topically applied substances.[35] The microscopic anatomy of a pig ear cross-section and pig ear skin can be found in Figure S1. The skin layers most relevant for this study are the top, the stratum corneum, the viable epidermis (consisting of stratum granulosum, stratum spinosum, and stratum basale), and the dermis.

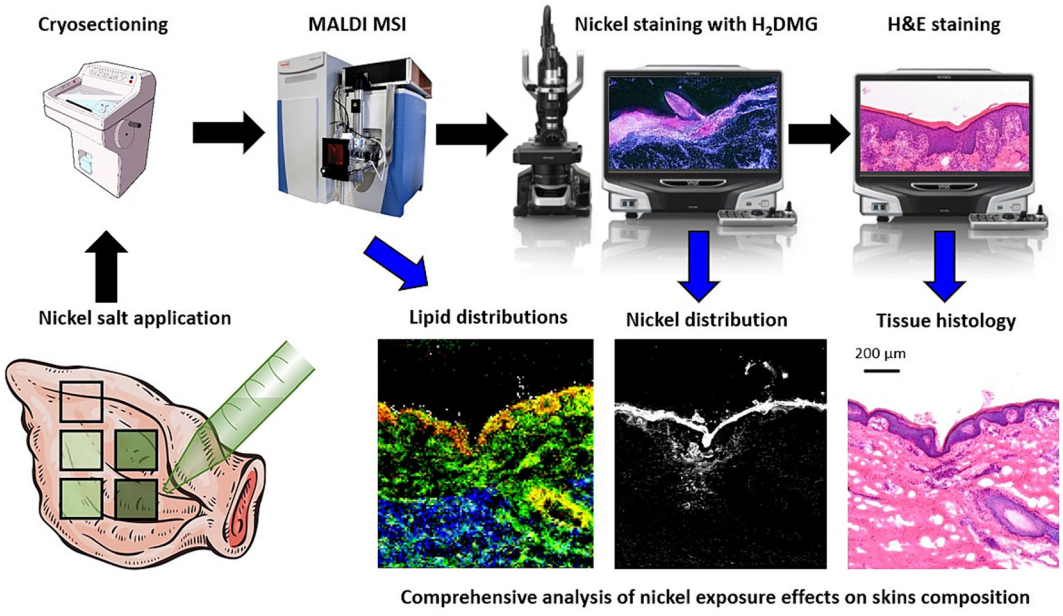

FIGURE 1 Experimental workflow illustrating the methodologies employed to investigate the effects of nickel exposure on skin. The study utilized ex vivo fresh porcine ear skin treated with nickel sulfate hexahydrate solutions of varying concentrations. After incubation, punch biopsies were taken, and tissues were processed for metabolomic and lipidomic analysis. MALDI MSI was used to examine metabolomic changes in skin cross-sections. Then, H_2DMG and H&E staining were employed to visualize nickel penetration and assess tissue morphology, respectively, by using a light microscope. LC-MS/MS was used for reliable lipid identification allowing lipid class and fatty acid assignment (not shown). [Color figure can be viewed at wileyonlinelibrary.com]

The method for visualizing nickel penetration into pig skin using light microscopy is based on the complexation of H_2DMG with Ni^{2+} ions, forming nickel dimethylglyoxime square planar complexes $(Ni(HDMG)_2)$ of pink color and low solubility in water (Figure S2a).[31] The reaction was first described in 1905 by L. Tschugajew and is a standard analytical method in classical qualitative and quantitative analysis,[36] which is here applied for tissue staining. The semiquantitative performance of the H_2DMG staining method for tissue sections was evaluated for various nickel concentrations and biological replicates.

The workflow implemented to depict and measure the intensity of the pink color resulting from $Ni(HDMG)_2$ in the skin sections is outlined in Figure S2b. Initially, high-resolution images of samples treated with different nickel concentrations (0, 17, 84, and 167 $\mu g/cm^2$) and stained by H_2DMG were captured by a light microscope under standardized lighting and magnification (250x). All images were converted to the same format (JPEG), maintaining consistent dimensions to ensure accurate comparison. Next, ImageJ software was used to split the images into red, green, and blue channels. To eliminate background interference from the tissue, the green channel was subtracted from the red channel (containing the $Ni(HDMG)_2$ signal). Finally, the total area and mean intensity of the derived gray-scale images showing only $Ni(HDMG)_2$ signal were measured, and the sum intensity was calculated.

Figure 2A shows the sum intensity of the $Ni(HDMG)_2$ complex for one biological replicate but three technical replicates, depending on the topically applied nickel concentration. The corresponding gray-scale images showing the distribution of $Ni(HDMG)_2$ in the skin cross-sections (one technical replicate) are depicted in Figure 2B. The sum intensity of $Ni(HDMG)_2$ increased linearly with Ni^{2+} concentration, with the highest intensity observed in the sample treated with 167 $\mu g/cm^2$ Ni^{2+} ($R^2 = 0.9292$). For concentrations up to 84 $\mu g/cm^2$, the applied nickel ions were predominately accumulated in the stratum corneum and barely detected in the viable epidermis. Figure S3 shows an overlay of $Ni(HDMG)_2$ distribution and H&E staining of the same skin cross-section treated with 84 $\mu g/cm^2$ Ni^{2+}. In addition, the identity of the $Ni(HDMG)_2$ complex and its distribution in the skin cross-section was confirmed by positive-ion

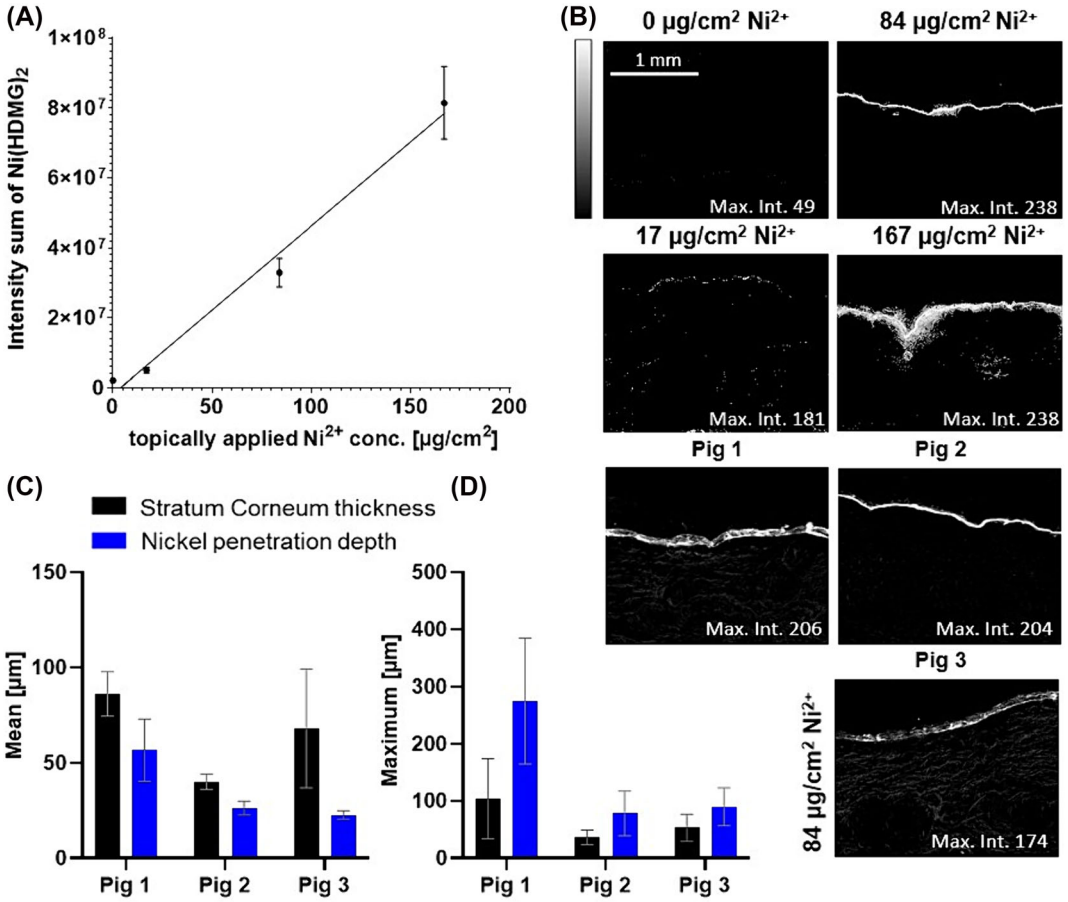

FIGURE 2 (A) Intensity sum of $Ni(HDMG)_2$ complex for control and samples treated with 17, 84, and 167 $\mu g/cm^2$ of Ni^{2+} (one biological, three technical replicates), (B) corresponding $Ni(HDMG)_2$ images of the samples (one technical replicate is shown), (C) mean stratum corneum thickness (black) and mean nickel penetration depth (blue) for three biological replicates treated with 84 $\mu g/cm^2$ nickel ions (three technical replicates per biological replicate), (D) maximum nickel penetration depth and corresponding stratum corneum thickness for three biological replicates treated with 84 $\mu g/cm^2$ nickel ions (three technical replicates per biological replicate) as well as corresponding $Ni(HDMG)_2$ images of the samples (one technical replicate is shown). Error bars represent standard deviation. [Color figure can be viewed at wileyonlinelibrary.com]

mode MALDI MSI. The $[Ni(HDMG)_2 + H]^+$ ion was observed readily at *m/z* 289.0440 with the expected isotopic pattern of a nickel ion. Microscopic and MALDI MS images revealed the same $Ni(HDMG)_2$ complex distribution in the stratum corneum (Figure S4). At 167 μg/cm^2 Ni^{2+} application, nickel ions penetrated deeper into the skin and were more often found in the viable epidermis and, to a small extent, in the dermis.

The nickel penetration depth was determined from the $Ni(HDMG)_2$ images of 84 μg/cm^2 Ni^{2+} treated skin samples (three technical replicates of three biological replicates) and compared to the stratum corneum thickness (Figure 2C,D). The $Ni(HDMG)_2$ distribution was strongly associated with the stratum corneum in all three biological replicates. Some penetration of nickel ions into the viable dermis was observed in one biological replicate. No $Ni(HDMG)_2$ signal was detected in the control skin cross-sections. The mean penetration depth of nickel ions was found to be lower than the mean thickness of the stratum corneum in each biological replicate ($n = 3$) (Figure 2C). However, there were severe differences in the mean stratum corneum thickness (86, 40, and 68 μm) and nickel penetration depths (57, 26, and 23 μm) for different biological replicates. The maximum penetration depth of nickel ions was found to be, on average, about 2.3 times larger than the stratum corneum thicknesses at these measurement points, showing that trace levels of nickel ions cross the skin barrier, reaching viable epidermis and even dermis (Figure 2D).

Overall, the data supports the method's effectiveness in detecting and quantifying nickel penetration. Compared to previous studies utilizing techniques such as TOF SIMS and ICP MS, the method developed in this study offers fast and cost-saving insights into nickel penetration mechanisms. Specifically, it provides valuable information on the localization of nickel within the skin's outermost layer.

3.2 | Nickel-induced metabolomic and lipidomic changes in pig ear skin

Metabolites and lipids play a major role in the function of skin. Alterations to the metabolomic and lipidomic composition of the skin have been associated with various skin diseases. Nickel-induced lipidomic changes in the stratum corneum and viable epidermis have focused so far on MAGs, DAGs, and ceramides. In our study, untargeted metabolomic and lipidomic analyses using MALDI MSI in the positive-ion mode were performed on an ex vivo porcine ear skin model with a spatial resolution of 10 μm. Cross-sections of pig ear skin from three biological replicates treated with 84 μg/cm^2 nickel sulfate (topically applied) alongside untreated control pig ear skin were analyzed to discern the impact of nickel ion exposure on skin metabolite composition. The ion signals of the combined MALDI MSI data set (3 control+3 nickel-treated samples) were annotated using METASPACE. In total, 536 ion signals were annotated using the databases LIPIDMAPS, swiss lipids, Human Metabolome Data Base (HMBD), and BraChem with a mass tolerance of ± 3 ppm, a false discovery rate of 10% and the following quasi-molecular ion: $[M + H]^+$, $[M + Na]^+$, $[M + K]^+$, $[M + NH_4]^+$. In addition, lipid extracts were prepared from the same tissues and analyzed with untargeted LC–MS/MS in positive-ion mode. A total of 1,012 lipids were identified by LipidMatchflow and 1,063 by MSDial. *m/z* values of the ions signal annotated in the MALDI MSI data set with METASPACE were manually compared with m/z values found in the LC–MS/MS data set by LipidMatchflow and MSDial. Ninety-three *m/z* values were found in both data sets and subjected to further analysis. After MALDI MSI, nickel ion distributions in the analyzed skin cross-section were determined by its reaction with H_2DMG, and tissue histology was obtained by subsequent H&E staining. Figure 3 shows the results from MALDI MSI (a), nickel staining with H_2DMG (b), and H&E staining (c) for control and an 84 μg/cm^2 nickel-treated sample. For MALDI MSI (Figure 3A), three MS images (with a mass tolerance of ±3 ppm, normalized to the total ion count (TIC)) were overlaid using the three native color channels (red, green, and blue) to illustrate the histology of the skin. Molecular markers for skin tissue layers were: *m/z* 522.4880, Cer-NS(d17:1/16:1), $[M + H]^+$ (red) for the stratum corneum; *m/z* 760.5851, PC(16:0/18:1), $[M + H]^+$ (blue) for dermis; and *m/z* 716.5225, PE(16:0/18:2), $[M + H]^+$ (green) for the viable epidermis. These markers were found to be not influenced by the nickel treatment and reproduced well the histology of the skin cross-section as determined by H&E staining (Figure 3C). On the other hand, staining of the skin cross-sections with H_2DMG (Figure 3B) revealed nickel ion distribution strongly associated with the stratum corneum in the nickel-treated skin cross-section. In contrast, the control skin cross-section only showed some background noise. Figure 3D shows the number of identified lipid species per lipid class: ceramides (CER, 22), diacylglycerols (DAG, 4), phosphatidylcholines (PC, 31), phosphatidylethanolamines (PE, 10), sphingomyelins (SM, 12) and lysophosphatidylcholines (LPC, 9). Several lipid classes were readily accessible with MALDI MSI in positive-ion mode, ranging from small molecules like cholesterol at *m/z* 369.3515 to complex lipids such as TG (16:0/16:0/18:1) at *m/z* 855.7412. High mass accuracy and mass resolution of the MALDI MSI data in combination with LC–MS/MS data allowed the reliable identification of individual lipid species, including the assignment of fatty acids. The results from MALDI MSI, nickel staining with H_2DMG, and H&E staining for all three biological replicates are shown in Figure S5.

The MALDI MSI data set described above was subjected to semi-quantitative analysis to identify which nickel ion treatment affects lipids and metabolites. The TIC-normalized mean intensities of all 93 identified lipids and two amino acids, arginine and histidine (identified by on-tissue MS/MS), were obtained from similar tissue areas (about 20.000–25.000 pixels) defined in SCILS Lab for the three control skin cross-sections and the three nickel-treated cross-sections. For each metabolite and lipid, a t-test was performed for the control versus nickel-treated group using the extracted TIC-normalized mean intensity values. A *p*-value smaller than 0.05 was considered significant. In total, 17 compounds were significantly downregulated in nickel-treated pig ear skin compared to control pig ear skin.

Changes in the lipid content were observed in all analyzed tissue layers (stratum corneum, viable epidermis, and dermis) and were not

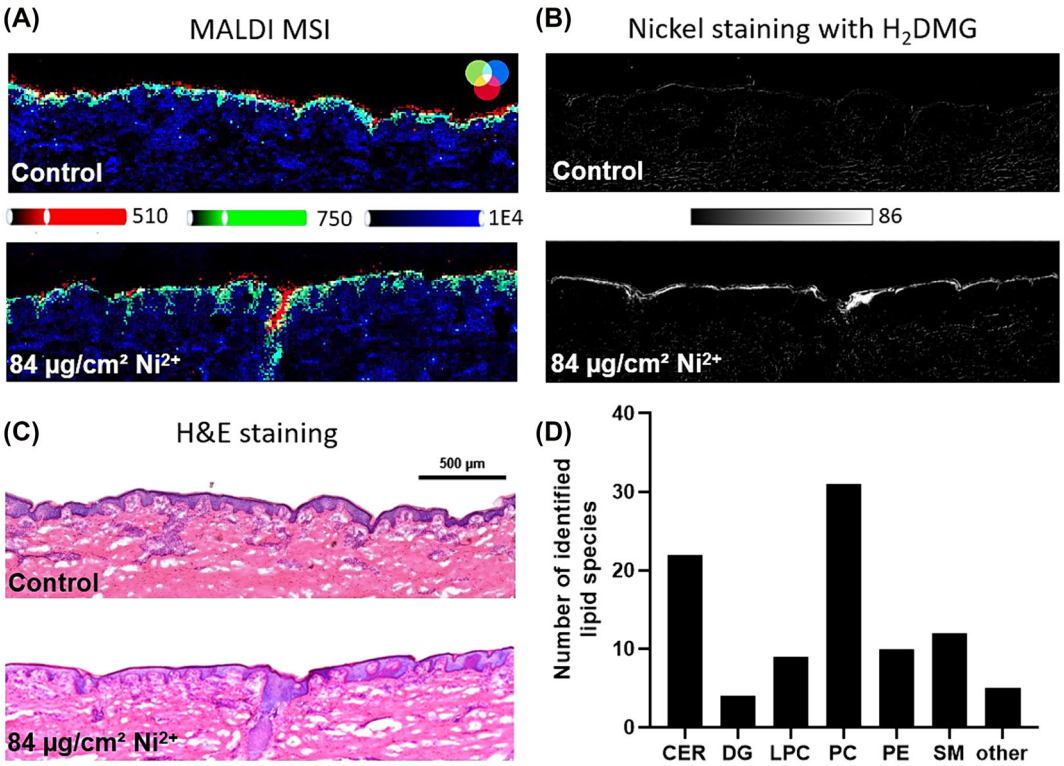

FIGURE 3 (A) RGB overlay images of three lipids measured by MALDI MSI with a step size of 10 µm in positive-ion mode from a control sample (290 × 99 pixels) and an 84 µg/cm^2 nickel-treated sample (298 × 92 pixels): *m/z* 522.4880, Cer-NS(d17:1/16:1), $[M + H]^+$ (red), marker for stratum corneum; *m/z* 760.5851, PC(16:0/18:1), $[M + H]^+$ (blue), marker for dermis; and *m/z* 716.5225, PE(16:0/18:2), $[M + H]^+$ (green), marker for the viable epidermis. The data was normalized to TIC. (B) Nickel distribution in a treated and a control sample was obtained by staining the samples with H_2DMG after MALDI MSI analysis. (C) H&E staining of a control sample and an 84 µg/cm^2 nickel-treated sample subjected previously to MALDI MSI and nickel staining with H_2DMG. d) Number of lipid species per lipid class detected by MALDI MSI and further validated by LC MS/MS in both nickel-treated and control groups. [Color figure can be viewed at wileyonlinelibrary.com]

limited to those areas directly penetrated by nickel ions, indicating that response mechanisms are not dependent on direct contact with the trigger. In Figure 4, PC (16:0/16:0) (A), SM(d17:1/19:0) (B), and arginine (C) were selected as molecular markers to depict the decrease of ion intensities within the dermis, viable epidermis, and stratum corneum, respectively, after nickel exposure. Bar charts in Figure 4D–F show the relative MALDI MSI intensities for all significantly down-regulated lipids and metabolites in relation to their main location (dermis, viable epidermis, and stratum corneum. The corresponding TIC-normalized ion images measured from three control and three nickel-treated samples can be found in Table S4. Notably, many of those lipids are structural lipids associated with the cell membranes belonging to sphingomyelin (SM) and phosphatidylcholine (PC) lipid classes. In addition, two PC species and four SM species feature odd-numbered fatty acids. The most abundant odd-numbered fatty acid features 17 carbons and one double bond. Fold-changes for downregulations ranged from 1.8 for arginine to 8.8 for SM(d17:1/22:0). Only arginine was found to be significantly downregulated in stratum corneum, but histidine and several ceramides showed a similar trend. Moreover, the observed downregulation of specific lipid species was dose-dependent. Figure S6 showed for one biological replicate decreasing signal intensities for arginine, histidine, SM(d18:1/20:0), and PC (16:0/18:0) with increasing nickel ion concentration (control, 42, 84, and 167 µg/cm^2). For the amino acids and ceramides, additionally, a localized effect in the stratum corneum was detected for one biological replicate with decreased molecular ion signals in areas with high nickel ion concentration (Figure S7). None of the 93 lipids semi-quantified in this study showed a significant up-regulation in the nickel-treated group.

Nickel ions, dissolved in water and deposited on the skin, first diffused into the stratum corneum. The middle of this layer is rich in arginine and serves as the first barrier for metal ions.[20] This barrier was also observed in our study for one biological replicate where the three stratum corneum layers were easily distinguished by microscopy, and most of the pink Ni(HDMG)$_2$ complex was found in the upper stratum corneum layer (Figure S8). Arginine is a natural moisturizing factor derived from filaggrin and is crucial to skin hydration. It was found in our study to be significantly downregulated in stratum corneum upon nickel treatment, which aligns with findings observed using chromium salts instead of nickel salts.[20] In addition, several ceramides showed a similar trend as arginine. Ceramides are considered as "mortar" (together with cholesterol and free fatty acids) between the corneocytes "bricks,"

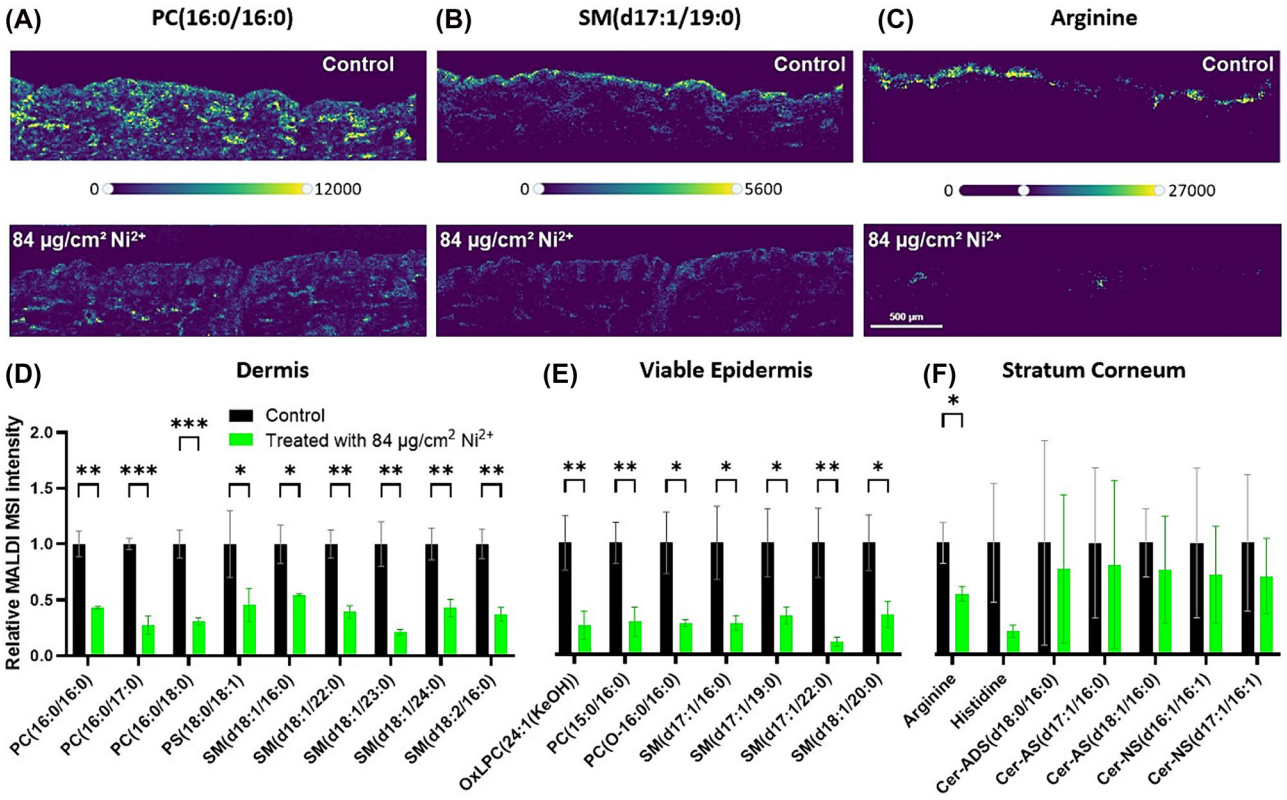

FIGURE 4 Metabolites and lipids downregulated by nickel exposure. (A–C) MALDI MSI images of downregulated molecular markers (A) for dermis: *m/z* 734.5694, (PC (16:0/16:0), $[M + H]^+$, (B) for viable epidermis: *m/z* 731.6062, SM(d17:1/19:0), $[M + H]^+$ and (C) stratum corneum: *m/z* 175.1190, arginine, $[M + H]^+$ (displayed *m/z* window: ±3 ppm). Depicted is a control skin sample with a size of 290 × 99 pixels and an 84 µg/cm^2 nickel-treated sample with a size of 298 × 92 pixels, acquired with a step size of 10 µm in positive-ion mode. (D) Relative MALDI MSI intensities of metabolites and lipids significantly downregulated by nickel treatment in (D) dermis, (E) viable epidermis, and (F) in stratum corneum. Relative MALDI MSI intensities were calculated by dividing mean intensities per sample by the average intensity of all control skin samples. Error bars show the standard deviation for three biological replicates. **p*-value > 0.05, ***p*-value > 0.01 and ****p*-value > 0.001. oxLPC(24:1(KeOH) refers to oxidized LPC, where KeOH represents a keto-hydroxy fatty acid. [Color figure can be viewed at wileyonlinelibrary.com]

which build together the water-permeability barrier of the skin. A decrease of arginine and ceramides upon nickel treatment thus suggests damage to the skin's barrier function. As demonstrated in this work, nickel ions penetrated in trace-level quantities into the viable epidermis and dermis, which is also in line with previous work. The lipid composition of the viable epidermis is dominated by phospholipids, especially phosphatidylcholines, and sphingomyelins. Phospholipids are membrane lipids. By their specific structure, they influence the fluidity and stiffness of the cell membranes and, therefore, their permeability. In addition, sphingomyelins form with cholesterol-specialized functional microdomains in the membrane, so-called "lipid rafts".[37] Besides that, sphingomyelins are considered a reservoir for bioactive lipids such as free fatty acids, ceramides, sphingosine, ceramide-1-phosphate, and sphingosine-1-phosphate.[37] Each of them has its own effect.[38] Metabolic pathways of ceramides, sphingomyelins, phosphatidylcholines, and their bioactive derivatives are highly interconnected. Changes in the concentration of any sphingolipid will result in changes in the concentration of other metabolites depending on the enzyme activity. Studies showed that any imbalance in ceramide/sphingomyelin concentrations is leveled out by keratinocytes in vitro in about three hours and that fatty acids can be transferred between SMs and PCs. Therefore, the observed downregulation of PCs and SMs in the viable epidermis might result from changes in the ceramide concentrations of the stratum corneum. On the other hand, bioactive products might be generated from PCs and SMs, which trigger further immune responses. The fatty acid composition of skin lipids is unique among mammalian tissues.[39] Skin is enriched in odd-chained and branched fatty acids. 9.4% of the total fatty acids in human skin lipids are odd-chain fatty acids (OCFA). In addition, a proportion of fatty acids are unusual long-chain (so-called very long-chain fatty acids (22–26 carbons, VLCFA) and ultra-long chain fatty acids (> 26 carbons, ULCFA)) and/or have a double bond in unusual places. Functionally, these fatty acids pose metabolic problems to pathogens and improve the survival of only compatible microorganisms. Further, VLCFA and ULCFA contribute to the rigidity and impermeability of membranes and, thus, to the skin's barrier function.[40] In our study, several phosphatidylcholines and sphingomyelins containing OCFAs and VLCFAs were found to be downregulated in viable epidermis and dermis. Possibly, they were degraded to bioactive lipids such as

ceramides and free fatty acids to restore skin barrier function or trigger further immune responses.

4 | CONCLUSION

Based on the comprehensive investigation conducted in this study, several key findings have emerged regarding the impact of nickel exposure on skin tissue, explicitly focusing on nickel penetration mechanisms and alterations in lipid composition. We have gained valuable insights into the intricate relationship between nickel exposure and skin physiology using advanced analytical techniques such as MALDI MSI, nickel staining with H_2DMG, and meticulous sample preparation methods. The development and validation of the nickel staining method with H_2DMG represent a significant advancement in the field, offering a cost-effective and rapid means of visualizing nickel penetration within the skin's outermost layer, the stratum corneum. Using this method, we can accurately detect the penetration of nickel ions by forming a pink complex of nickel bis (dimethylglyoximate), even at low concentrations. This method provides crucial information for understanding the mechanisms behind nickel-induced allergic reactions. The H_2DMG staining intensity consistently observed across different nickel concentrations highlights the reliability and reproducibility of this approach, making it a valuable tool for assessing various nickel exposure scenarios. Furthermore, our investigation into the metabolite profile of skin tissue following nickel exposure has revealed notable alterations in essential lipid and amino acid species, particularly sphingolipids, phosphatidylcholines, histidine, and arginine, which play crucial roles in maintaining skin structure and function. The observed decreases in specific lipid species in the stratum corneum, epidermis, and dermis suggest a disruption in the skin's barrier function in response to nickel exposure. These findings provide important insights into the potential mechanisms by which nickel allergy manifests and highlight the intricate interplay between metal exposure, lipid metabolism, and immune response in the skin. Overall, the findings of this study contribute to a deeper understanding of nickel-induced skin allergies and provide a foundation for further research to develop targeted diagnostic and therapeutic strategies for individuals with nickel sensitivities. By elucidating the complex interactions between nickel ions and skin tissue at the molecular level, we can pave the way for more effective approaches to managing and preventing nickel-related dermatological conditions. Future investigations should continue to explore the mechanisms underlying nickel penetration and its effects on skin lipid composition, aiming to improve patient care and quality of life for those affected by nickel allergies.

AUTHOR CONTRIBUTIONS

Conceptualization, A.R., S.Schu., Y.G. C.M.K., S.Sch. and B.S; methodology, A.R. and Y.G; software, A.R. and S.Schu; validation, S. Schu., C.M.K., B.S. and S.Sch.; formal analysis, A.R., S.Schu.; investigation, A.R.; resources, C.M.K., S.Sch. and B.S.; data curation, A.R. and S.Schu; writing—original draft preparation, A.R.; writing—review and editing, S.Schu., C.M.K. and B.S.; visualization, A.R. and S. Schu; supervision, S. Schu, S.Sch. and B.S.; funding acquisition, B.S. All authors have read and agreed to the published version of the manuscript.

ACKNOWLEDGMENTS

Financial support by the German Academic Exchange Service-Graduate School Scholarship Programme (DAAD-GSSP) "Chemistry for Life" and the Giessen Graduate Center for the Life Sciences GGL is gratefully acknowledged (A. R.). Technical support by Thermo Fisher Scientific GmbH (Bremen, Germany) and by TransMIT GmbH (Giessen, Germany) is gratefully acknowledged. Open Access funding enabled and organized by Projekt DEAL.

CONFLICT OF INTEREST STATEMENT

B.S. and C.M.K. are consultants of TransMIT GmbH (Giessen, Germany). The other authors declare no conflicts of interest.

DATA AVAILABILITY STATEMENT

The data presented in this study are public available at METASPACE online platform: https://metaspace2020.eu/project/Ni_pig_skin_24.

ORCID

Siegfried Schindler https://orcid.org/0000-0002-9991-9513
Bernhard Spengler https://orcid.org/0000-0003-0179-5653
Cornelia M. Keck https://orcid.org/0000-0001-8888-2340
Sabine Schulz https://orcid.org/0000-0002-6561-5562

REFERENCES

1. Martin SF, Rühl-Muth A-C, Esser PR. Orchestration of inflammation in contact allergy by innate immune and cellular stress responses. *Allergo J Int*. 2024;33(2):41-48. doi:10.1007/s40629-023-00275-4
2. El Ali Z, Gerbeix C, Hemon P, et al. Allergic skin inflammation induced by chemical sensitizers is controlled by the transcription factor Nrf2. *Toxicol Sci*. 2013;134(1):39-48. doi:10.1093/toxsci/kft084
3. Salazar F, Ghaemmaghami AM. Allergen recognition by innate immune cells: critical role of dendritic and epithelial cells. *Front Immunol*. 2013;4:356. doi:10.3389/fimmu.2013.00356
4. Tan C-H, Rasool S, Johnston GA. Contact dermatitis: allergic and irritant. *Clin Dermatol*. 2014;32(1):116-124. doi:10.1016/j.clindermatol.2013.05.033
5. Rustemeyer T. Immunological mechanisms in allergic contact dermatitis. *Curr Treat Options Allergy*. 2022;9(2):67-75. doi:10.1007/s40521-022-00299-1
6. Panickar KS, Bhathena SJ. *Control of Fatty Acid Intake and the Role of Essential Fatty Acids in Cognitive Function and Neurological Disorders*. In: Montmayeur J-P, le Coutre J, eds.; 2010, doi:10.1201/9781420067767-c18.
7. Glatz JFC. Challenges in fatty acid and lipid physiology. *Front Physiol*. 2011;2:45. doi:10.3389/fphys.2011.00045
8. Elias PM, Schmuth M. Abnormal skin barrier in the etiopathogenesis of atopic dermatitis. *Curr Opin Allergy Clin Immunol*. 2009;9(5):437-446. doi:10.1097/ACI.0b013e32832e7d36
9. Simpson EL, Chalmers JR, Hanifin JM, et al. Emollient enhancement of the skin barrier from birth offers effective atopic dermatitis prevention. *J Allergy Clin Immunol*. 2014;134(4):818-823. doi:10.1016/j.jaci.2014.08.005

10. Agrawal R, Woodfolk JA. Skin barrier defects in atopic dermatitis. *Curr Allergy Asthma Rep*. 2014;14(5):433. doi:10.1007/s11882-014-0433-9
11. Thyssen JP, Menné T. Metal allergy—a review on exposures, penetration, genetics, prevalence, and clinical implications. *Chem Res Toxicol*. 2010;23(2):309-318. doi:10.1021/tx9002726
12. Saito M, Arakaki R, Yamada A, Tsunematsu T, Kudo Y, Ishimaru N. Molecular mechanisms of nickel allergy. *Int J Mol Sci*. 2016;17(2):202. doi:10.3390/ijms17020202
13. Magnano GC, Marussi G, Crosera M, et al. Probing the effectiveness of barrier creams against human skin penetration of nickel powder. *Int J Cosmet Sci*. 2024;46(1):39-50. doi:10.1111/ics.12893
14. Basketter D. Nickel: Intrinsic skin sensitization potency and relation to prevalence of contact allergy. *Dermat Contact, Atopic, Occup Drug*. 2021;32(2):71-77. doi:10.1097/DER.0000000000000666
15. Yamaguchi HL, Yamaguchi Y, Peeva E. Role of innate immunity in allergic contact dermatitis: an update. *Int J Mol Sci*. 2023;24(16):12975. doi:10.3390/ijms241612975
16. Knox S, Hagvall L, Malmberg P, O'Boyle NM. Topical application of metal allergens induces changes to lipid composition of human skin. *Front Toxicol*. 2022;4(August):867163. doi:10.3389/ftox.2022.867163
17. Borodzicz S, Rudnicka L, Mirowska-Guzel D, Cudnoch-Jedrzejewska A. The role of epidermal sphingolipids in dermatologic diseases. *Lipids Health Dis*. 2016;15(1):13. doi:10.1186/s12944-016-0178-7
18. Choi MJ, Maibach HI. Role of ceramides in barrier function of healthy and diseased skin. *Am J Clin Dermatol*. 2005;6(4):215-223. doi:10.2165/00128071-200506040-00002
19. Franco J, Rajwa B, Ferreira CR, Sundberg JP, HogenEsch H. Lipidomic profiling of the epidermis in a mouse model of dermatitis reveals sexual dimorphism and changes in lipid composition before the onset of clinical disease. *Metabolites*. 2020;10(7):299. doi:10.3390/metabo10070299
20. Kubo A, Ishizaki I, Kubo A, et al. The stratum corneum comprises three layers with distinct metal-ion barrier properties. *Sci Rep*. 2013;3(1):1731. doi:10.1038/srep01731
21. Tanojo H, Hostýnek JJ, Mountford HS, Maibach HI. In vitro permeation of nickel salts through human stratum corneum. *Acta Derm Venereol*. 2021;81(212 SE-Articles):19-23. doi:10.1080/000155501753279596
22. Malmberg P, Guttenberg T, Ericson MB, Hagvall L. Imaging mass spectrometry for novel insights into contact allergy—a proof-of-concept study on nickel. *Contact Dermatitis*. 2018;78(2):109-116. doi:10.1111/cod.12911
23. Hagvall L, Pour MD, Feng J, Karma M, Hedberg Y, Malmberg P. Skin permeation of nickel, cobalt and chromium salts in ex vivo human skin, visualized using mass spectrometry imaging. *Toxicol In Vitro*. 2021;76(July):105232. doi:10.1016/j.tiv.2021.105232
24. Hart PJ, Francese S, Claude E, Woodroofe MN, Clench MR. MALDI-MS imaging of lipids in ex vivo human skin. *Anal Bioanal Chem*. 2011;401(1):115-125. doi:10.1007/s00216-011-5090-4
25. Roy S, Touboul D, Brunelle A, et al. Application à la maladie de Fabry. *Ann Pharm Fr*. 2006;64(5):328-334. doi:10.1016/S0003-4509(06)75325-1
26. Harvey A, Cole LM, Day R, et al. MALDI-MSI for the analysis of a 3D tissue-engineered psoriatic skin model. *Proteomics*. 2016;16(11–12):1718-1725. doi:10.1002/pmic.201600036
27. Kompauer M, Heiles S, Spengler B. Atmospheric pressure MALDI mass spectrometry imaging of tissues and cells at 1.4-μm lateral resolution. *Nat Methods*. 2016;14(1):90-96. doi:10.1038/nmeth.4071
28. Kompauer M, Heiles S, Spengler B. Chemical and topographical 3D surface profiling using atmospheric pressure LDI and MALDI MS imaging. *Protoc Exch Published*. 2017;18. doi:10.1038/protex.2017.103
29. Pelikh O, Pinnapireddy SR, Keck CM. Dermal penetration analysis of curcumin in an ex vivo porcine ear model using epifluorescence microscopy and digital image processing. *Skin Pharmacol Physiol*. 2021;34(5):281-299. doi:10.1159/000514498
30. Bouschen W, Schulz O, Eikel D, Spengler B. Matrix vapor deposition/recrystallization and dedicated spray preparation for high-resolution scanning microprobe matrix-assisted laser desorption/ionization imaging mass spectrometry (SMALDI-MS) of tissue and single cells. *Rapid Commun Mass Spectrom*. 2010;24(3):355-364. doi:10.1002/rcm.4401
31. Julander A, Skare L, Vahter M, Lidén C. Nickel deposited on the skin–visualization by DMG test. *Contact Dermatitis*. 2011;64(3):151-157. doi:10.1111/j.1600-0536.2010.01856.x
32. Schneider CA, Rasband WS, Eliceiri KW. NIH image to ImageJ: 25 years of image analysis. *Nat Methods*. 2012;9(7):671-675. doi:10.1038/nmeth.2089
33. Matyash V, Liebisch G, Kurzchalia TV, Shevchenko A, Schwudke D. Lipid extraction by methyl-tert-butyl ether for high-throughput lipidomics. *J Lipid Res*. 2008;49(5):1137-1146. doi:10.1194/jlr.D700041-JLR200
34. Koelmel JP, Kroeger NM, Ulmer CZ, et al. LipidMatch: an automated workflow for rule-based lipid identification using untargeted high-resolution tandem mass spectrometry data. *BMC Bioinformatics*. 2017;18(1):331. doi:10.1186/s12859-017-1744-3
35. Khiao In M, Richardson KC, Loewa A, Hedtrich S, Kaessmeyer S, Plendl J. Histological and functional comparisons of four anatomical regions of porcine skin with human abdominal skin. *Anat Histol Embryol*. 2019;48(3):207-217. doi:10.1111/ahe.12425
36. Tschugaeff L. Ueber ein neues, empfindliches Reagens auf nickel. *Berichte der Dtsch Chem Gesellschaft*. 1905;38(3):2520-2522. doi:10.1002/cber.19050380317
37. Wanner R, Peiser M, Wittig B. Keratinocytes rapidly readjust ceramide–sphingomyelin homeostasis and contain a phosphatidylcholine–sphingomyelin transacylase. *J Invest Dermatol*. 2004;122(3):773-782. doi:10.1111/j.0022-202X.2004.22340.x
38. Vietri Rudan M, Watt FM. Mammalian epidermis: a compendium of lipid functionality. *Front Physiol*. 2022;12:12. doi:10.3389/fphys.2021.804824
39. Nicolaides N. Skin lipids: their biochemical uniqueness. *Science (80-)*. 1974;186(4158):19-26. doi:10.1126/science.186.4158.19
40. Zwara A, Wertheim-Tysarowska K, Mika A. Alterations of ultra long-chain fatty acids in hereditary skin diseases—review article. *Front Med*. 2021;8(August):730855. doi:10.3389/fmed.2021.730855

SUPPORTING INFORMATION

Additional supporting information can be found online in the Supporting Information section at the end of this article.

How to cite this article: Rezaei A, Ganashalingam Y, Schindler S, Spengler B, Keck CM, Schulz S. Metabolipidomic changes induced by dermal nickel penetration determined in an ex vivo porcine ear skin model. *Rapid Commun Mass Spectrom*. 2024;38(20):e9891. doi:10.1002/rcm.9891